



LAWRENCE
LIVERMORE
NATIONAL
LABORATORY

Process for rapid detection of fratricidal defects on optics using Linescan Phase Differential Imaging

F. L. Ravizza, M. C. Nostrand, L. M. Kegelmeyer,
R. A. Hawley, M. A. Johnson

December 1, 2009

Boulder Damage Symposium
Boulder, CO, United States
September 21, 2009 through September 23, 2009

Disclaimer

This document was prepared as an account of work sponsored by an agency of the United States government. Neither the United States government nor Lawrence Livermore National Security, LLC, nor any of their employees makes any warranty, expressed or implied, or assumes any legal liability or responsibility for the accuracy, completeness, or usefulness of any information, apparatus, product, or process disclosed, or represents that its use would not infringe privately owned rights. Reference herein to any specific commercial product, process, or service by trade name, trademark, manufacturer, or otherwise does not necessarily constitute or imply its endorsement, recommendation, or favoring by the United States government or Lawrence Livermore National Security, LLC. The views and opinions of authors expressed herein do not necessarily state or reflect those of the United States government or Lawrence Livermore National Security, LLC, and shall not be used for advertising or product endorsement purposes.

Process for rapid detection of fratricidal defects on optics using Linescan Phase Differential Imaging

Frank L. Ravizza, Michael C. Nostrand, Laura M. Kegelmeyer, Ruth A. Hawley and Michael A. Johnson

Lawrence Livermore National Laboratory,
7000 East Avenue, L-491, Livermore, CA 94550-9234 USA

ABSTRACT

Phase-defects on optics used in high-power lasers can cause light intensification leading to laser-induced damage of downstream optics. We introduce Linescan Phase Differential Imaging (LPDI), a large-area dark-field imaging technique able to identify phase-defects in the bulk or surface of large-aperture optics with a 67 second scan-time. Potential phase-defects in the LPDI images are identified by an image analysis code and measured with a Phase Shifting Diffraction Interferometer (PSDI). The PSDI data is used to calculate the defects potential for downstream damage using an empirical laser-damage model that incorporates a laser propagation code. A ray tracing model of LPDI was developed to enhance our understanding of its phase-defect detection mechanism and reveal limitations.

1.0 INTRODUCTION

Limiting laser-induced damage to valuable optics is critical to sustainable operation of high-power lasers, such as the National Ignition Facility (NIF). The NIF is designed to deliver 1.8-MJ of energy and 500-TW of peak-power to a target using 192 precisely timed, focused and temporally shaped 351-nm laser pulses.¹ Economical design requires optic apertures be exposed to light irradiances very near to where damage occurs. To avert damage, the beam must be uniform and free of regions of elevated irradiance, or *hot spots*. Diffraction of the wavefront through localized phase-defects on optics can generate hot spots that result in damage to downstream optics, a phenomenon termed *fratricide*, illustrated in Fig. 1. Nonlinear optical processes such as *self-focusing* and *conjugate imaging* can also cause hot spots.² Phase-defects can appear in the bulk or surface of fused silica optics during finishing or sol-gel coating. Phase-defects can be difficult to detect with conventional inspection techniques since they do not scatter light into a large solid-angle. Fratricidal phase-defect (FPD) are especially insidious when they remain undiscovered until after fratricide occurs. An appropriate strategy is to screen optics for FPD with a non-destructive process prior to installation.

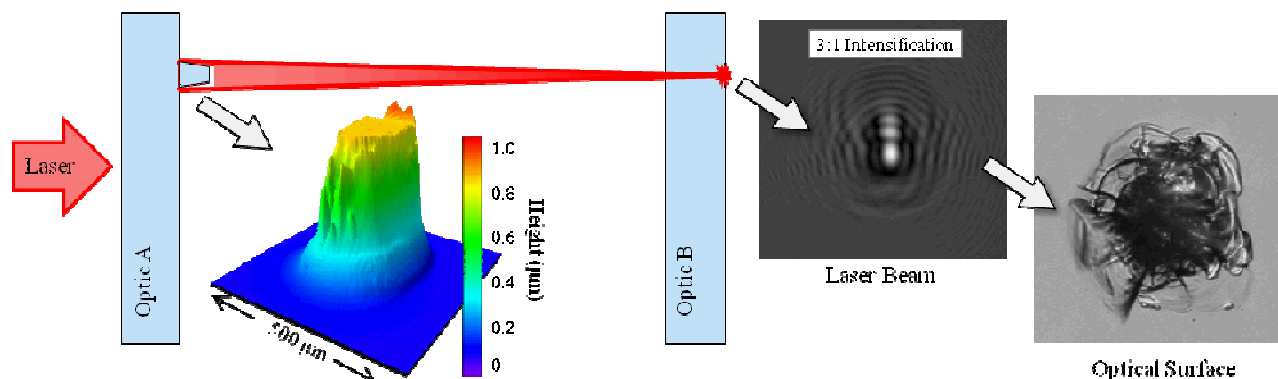


Figure 1: Fratricide, illustrated here, originated from a phase-defect on Optic A generated during surface finishing, which intensified the wavefront 20-cm downstream to result in a 300-μm diameter damage site to Optic B.

The first FPD screening system, called the Inclusion Mapping System (IMS)³, was developed in 2004 at LLNL. IMS was designed to exploit the light intensifying behavior of phase-defects by rendering them as bright spots when illuminated with a condensed backlight and imaged slightly away from the object plane. Condensing lens size limitations required that IMS map large-aperture optics (400x400-mm²) in nine sub-apertures. This produced images with excellent spatial resolution (25- μ m/pixel), but this largely contributed to an unacceptable optic processing rate of 3-hr/optic.

2.0 NEW PROCESS DEVELOPMENT

To improve the optic processing rate, two full-aperture imaging systems were initially considered: bright-field IMS and dark-field (Schlieren). The dark-field was the preferred technique based on results from our in-situ Final Optics Damage Inspection (FODI)⁴ system that demonstrated excellent sensitivity to phase-defects. The proposed dark-field system required collimated back illumination and 1:1 imaging using two full-aperture (>565-mm dia.) fast focusing ($>f/2$) condensing lenses. The challenges associated with designing these extreme optical components in the space available led us to consider a new full-aperture imaging concept that could eliminate condensing lenses by emulating a 2-D illumination field using linescan imaging and a linear light source.

Linescan imaging is a technique commonly employed in photocopiers and fax machines in which images are digitized one line at a time by a spatially and temporally synchronized linear sensor that it is scanned over the image plane. Linescan imaging is implemented in LPDI by translating the optic under investigation and fixing the light source, camera lens and sensor. Development of a model for this new imaging technique revealed its images are related to the partial derivative of an objects phase caused by off-axis alignment of the light source.

3.0 LPDI CONFIGURATION

LPDI has four components: linear light source, linear translation stage, camera lens and linear sensor, as illustrated in Fig. 2. The linear light source is a Schott Lightline, a light guide composed of hundreds of identical fiber optics tightly packed into a circular bundle for efficient coupling to a light source. At the output, fibers are aimed in the z -direction and evenly distributed into an 82-cm line array centered on the test optic aperture that is oriented parallel to the y -axis. Individual fiber core diameters are small enough to be treated as point sources. Light is generated from a halogen lamp that emits incoherent photons with random polarization.

The camera lens is a Rodenstock Apo-Sironar-S 210mm $f/5.6$ produced by LINOS Photonics GmbH stopped down to an aperture of $f/16$ (to increase depth of field) that is installed in a field view camera produced by Wista. Images are recorded by a BetterLight, Inc Super-8k-HS digital scan back using a 16-bit Kodak KLI-8023 linear CCD array containing 3x8000 9- μ m pixels. The 3 columns of pixels are oriented parallel to the y -axis and record the primary colors red, green and blue, however only the green channel that is most sensitive to white light is used. The camera lens is focused on the optical center of the optic under test, with a magnification of -0.16 to produce a pixel size at the object plane of 56- μ m and a 448-mm vertical field of view. During line scanning the sensor is fixed near the optical axis and captures images with a 1:1 aspect ratio in 67 seconds using a 120-Hz line sampling rate.

Linescanning of the test optic occurs in the positive x -direction in the xz -plane (top view). The light source short axis is illustrated in the top view as a singular point source which exhibits a radiation pattern characteristic of a fiber optic numerical aperture that is displaced from the optical axis by distance x_d . Rays transmitted through the test optic have a non-zero angle of incidence equal to α with respect to the object plane. The long axis of the light source is illustrated in the yz -plane (side view) as a linear array of point sources extending over the full-aperture of the test optic. In the top view, rays are imaged to the short axis of the linear sensor by the camera lens from a fixed object location on the optical axis. The long axis of the linear sensor, illustrated in the side view, records rays imaged in a field of view covering the test optic aperture.

Repeatable dark-field alignment is referenced from bright-field by locating the light source in the x -axis where the integrated sensor signal is maximized. To account for the background refraction of the optic, alignment is performed with the camera lens imaging the light source directly through the optic under test. For this reason, LPDI cannot be used on optics with nonplanar surface, such as lenses, in the configuration described here. Theoretically, it is possible to measure nonplanar surfaces by translating the light source along the x -axis in parallel with the test optic to account for

the variable refraction of the test lens. Dark-field imaging can now be repeatably configured by displacing the light source in the x -axis by distance x_d . Finally, camera focus is returned to the optical center of the test optic. Using a light source positioner with 10- μm resolution, an α alignment precision of 18- μrad is possible, however 180- μrad precision is acceptable.

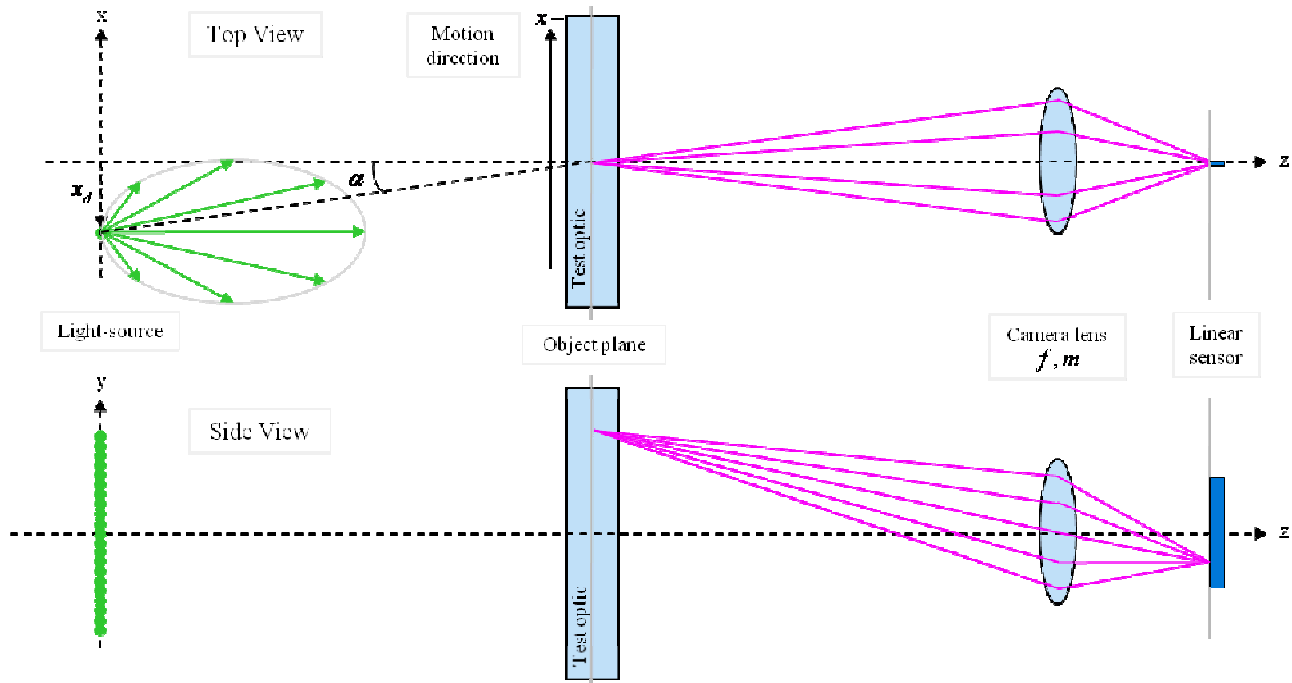


Figure 2: The upper and lower figures illustrate the LDPI configuration viewed in the xz - and yz -plane respectively.

LPDI only detects objects which change the direction of illumination. Objects which predominantly forward-scatter light, such as phase-defects, will produce the most intense signal, as opposed to amplitude objects which back-scatter light into a large solid-angle. We define *contrast* as the ratio of the phase-defect and background signals. As α increases the background signal is reduced to produce the dark-field. Contrast is possible since the phase-defect signal decreases slower than the background signal. Optimal contrast is best found empirically by measuring it as a function of α using a reference optic containing previously characterized phase-defects of interest. For our configuration, a typical α is 3-mrad. Maximum peak contrast is improved by using a light source with a minimum x -axis fiber distribution to minimize the background signal.

4.0 OBJECT IDENTIFICATION

Figure 3 shows an LPDI image of a fused silica vacuum window, on which we discovered the FPD from Fig. 1, analyzed using a Local Area Signal-to-Noise Ratio (LASNR) segmentation algorithm developed at LLNL⁵. The image analysis software identifies objects in the LPDI image by reporting each detections xy -coordinate, brightest pixel value (P_{max}), integrated pixel value (P_{int}) and serialized *Defect ID*, see *Image Analysis Results* in Table 1. Also shown in Fig. 3 are LPDI and IMS image crops of the surface phase-defect from Fig. 1 to show their respective contrasts of 30:1 and 4:1. Image contrast of the full-size image was enhanced to reveal the weak LPDI background signal that is recognized as horizontal banding caused by an irregular amplitude distribution of fibers in our light source. This relatively low background signal (<1000 pixel value) allows LPDI and other large-area dark-field imaging systems that spatially filter the background illumination, to identify phase-defect with superior contrast to bright-field systems that directly measure light intensification. LPDI has the sensitivity to detect benign phase-defects, in a signal pixel, that have an optical path difference as small 100-nm and lateral size of 50- μm . Defects smaller than the spatial resolution of the camera can be detected as long as the irradiance of their small-angle light scatter signal imaged to a pixel exceeds the background.

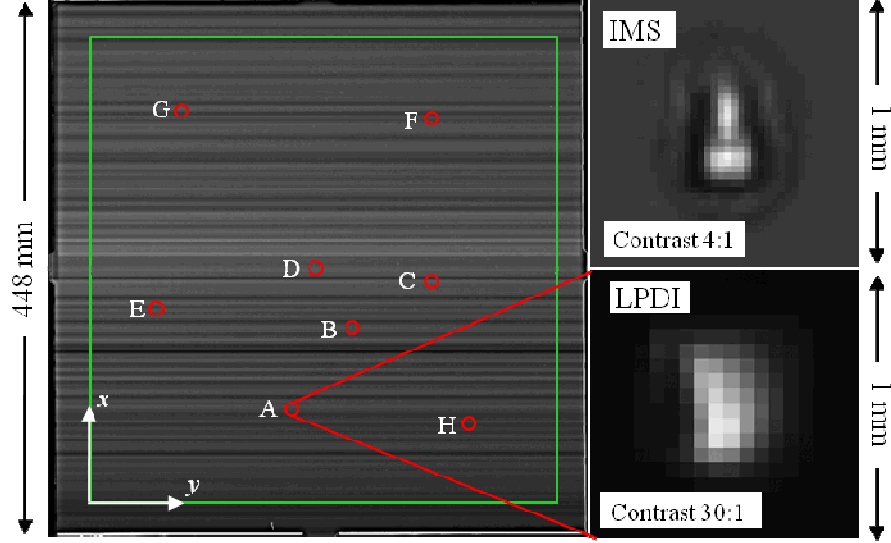


Figure 3: (left) LPDI image of fused silica vacuum window, showing 8 potential FPD sites, with enhanced contrast to reveal horizontal banding in the LPDI background. The phase-defect from Fig. 1 is shown in 1x1-mm² field of view image crops of LPDI (lower-right) and IMS (upper-left). LPDI and IMS detected the phase-defect with 30:1 and 4:1 contrast. Objects identified by the image analysis code are shown in Table 1.

Image Analysis Results					Fratricide Model Results		
Defect ID	x (mm)	y (mm)	P_{max} (counts)	P_{int} (counts)	I_{peak} (GW·cm ⁻²)	<N>	Pass / Fail
A	121	62	29607	213504	19.4	1878.322	Fail
B	140	187	20287	84621	45.31	63.984	Fail
C	285	209	19446	65741	20.21	53.896	Fail
D	189	199	29597	171890	112.8	1.583	Fail
E	50	183	9379	95027	8.03	0.001	Pass
F	315	265	5617	125488	6.48	0	Pass
G	68	283	13628	78612	7.31	0	Pass
H	273	50	5652	86264	4.98	0	Pass

Table 1: Image analysis and propagation code results are shown for the LPDI image in Fig 3.

4.1 OBJECT CHARACTERIZATION

LPDI images cannot be used to directly assess fratricide potential. However, the list of identified objects does provide a map to potential FPD on the optic to locate and measure them with a high resolution Phase-shifting Diffraction Interferometer (PSDI)⁶. The PSDI data is used by an empirical *Fratricide Model* to determine the potential for bulk or surface damage on downstream optics based on results from a laser propagation code⁷ that calculates the down-stream laser energy density (fluence) and peak irradiance (I_{peak}). The modeled fluence data is used, along with measurements of the surface damage initiation density as a function of fluence⁸, to calculate the expected number of surface damage initiations (<N>), while I_{peak} determines the onset of *filamentation*⁹ bulk damage. The entire optic fails if <N> or I_{peak} exceed a specified value. Passing and failing flaws identified in the LPDI image from Fig. 3 are available under *Fratricide Model Results* in Table 1.

Table 1 indicates half of the defects identified in the LDPI image from Fig. 3 passed fratricide analysis; these were *false-positives*. Considering fratricide depends on the location of the defect in the optical system and nonlinear optical processes which LPDI cannot account for, it can be expected that not all identified objects will fail. To reduce the time processing false-positives, we determined the LPDI *noise floor* by correlating the image analysis metrics P_{max} and P_{int} to the *Pass/Fail* results. Figures 4 show the relationship of P_{max} and P_{int} values for a large set of passing and failing defects.

Failure probability is shown in Fig. 5 to increase as a function of $P_{max}^{2.9}$. This statistical analysis was used to set a conservative noise floor based on a P_{max} value of 2700 where failure probability is very near to zero. This reduced the number of false-positives by 60% and reduced the overall processing time by 15 minutes per optic. A schematic view of the complete LPDI process is shown in Fig. 6.

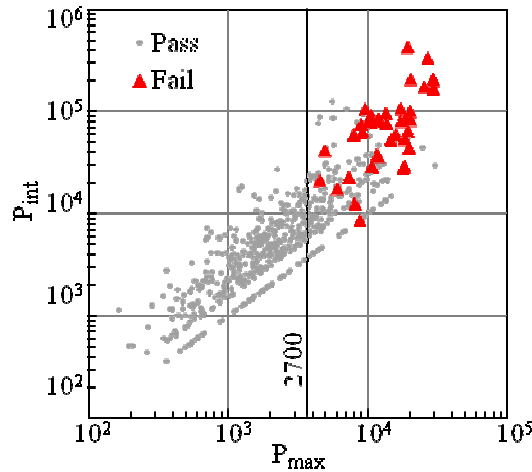


Figure 4: Scatter plot of P_{max} and P_{int} shows the distribution of failing and passing defects. All failing defects exceed the 2700 P_{max} threshold. Points forming a line are single pixel detections.

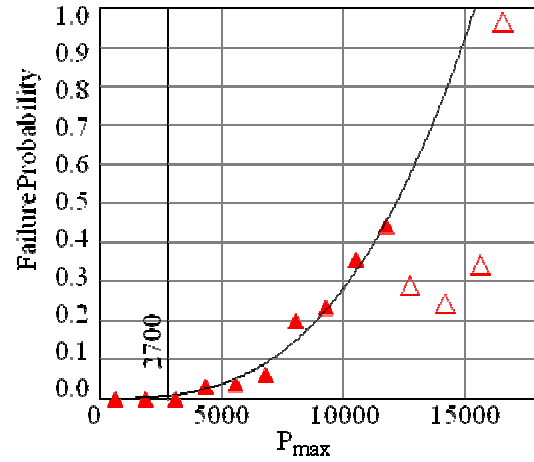


Figure 5: The failure probability as a function of P_{max} was calculated by binning the data from Fig. 4. The failure probability of each bin was fit to a power function ($P_{max}^{2.9}$). The sampling size in bins above 11780 was low (shown as open triangle points).

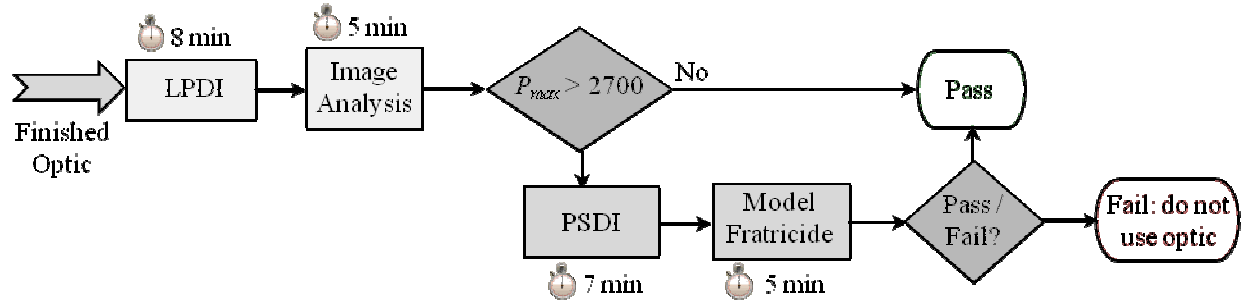


Figure 6: Schematic view of the complete process used to screen optics for FPD using LPDI and the average processing time for each step. On average the total processing time per optic is 25 minutes. Total processing time depends on the number of identifications in the LPDI image with $P_{max} > 2700$ which require PSDI measurement and fraticide modeling.

5.0 LPDI THEORY

Linescan Phase Differential Imaging only receives a signal from objects that perturb the illumination into a small solid angle determined by the camera lens effective numerical aperture. This effect is demonstrated with the aid of ray tracing software in two cases. In the first case, the test optic contains a phase-object, modeled as a micro-lens, and for the second case, the optic is free of any defect (Fig. 7). The first case shows the phase-defect forward-scatters light into a small angle (Fig. 7A) causing light *scattered* by the defect to be imaged onto the linear sensor (Fig. 7B). The second case shows pristine material does not scatter light (Fig. 7C), and light is not imaged to the linear sensor (Fig. 7D).

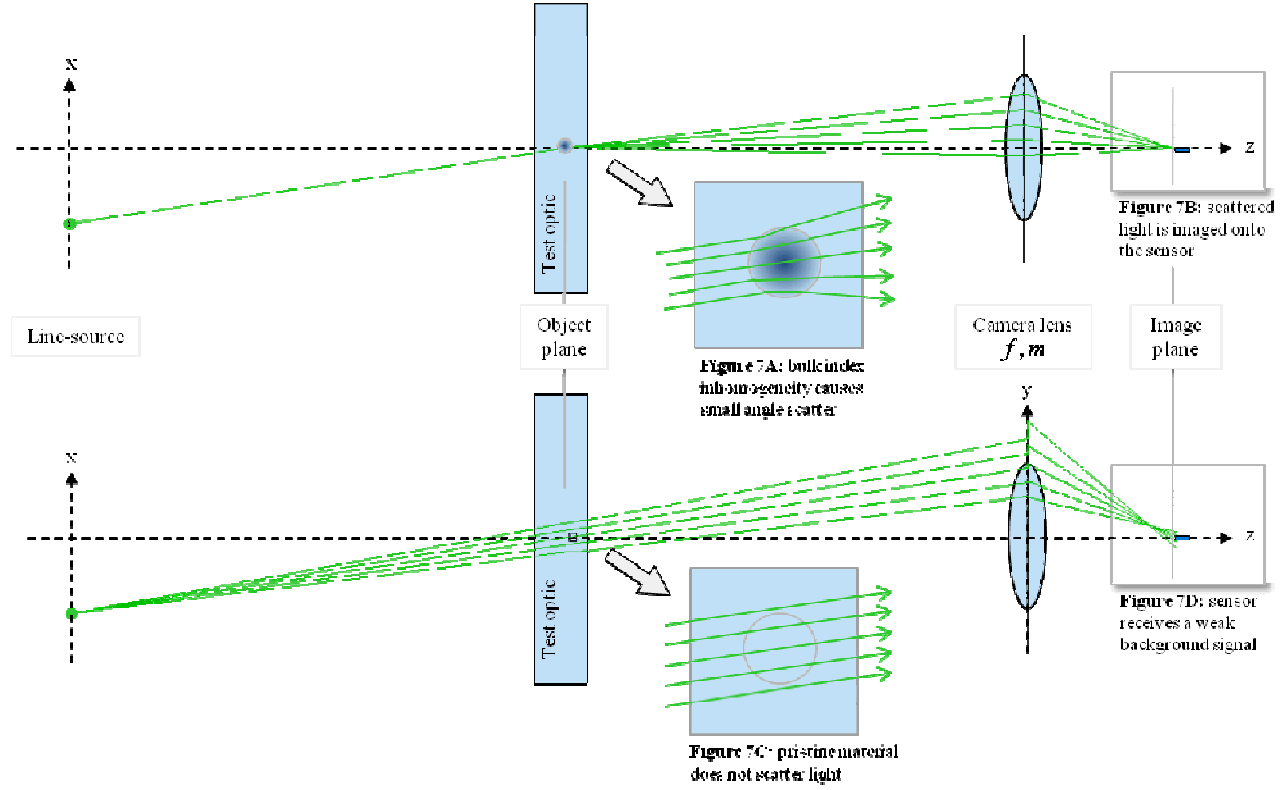


Figure 7: The upper and lower figures show LPDI systems measuring an optic containing a phase-defect and one of pristine material. The illumination ray bundle used for the pristine case is intentionally broader to show light is not focused onto the sensor.

Geometry determines the light collecting property of the lens which we define as minimum and maximum collection angles, θ_+ and θ_- respectively, see Fig. 8.

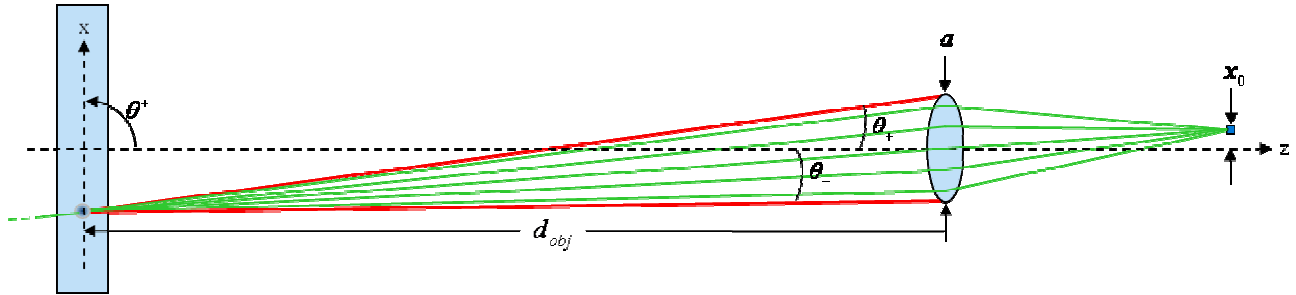


Figure 8: The range of rays angles imaged to the linear sensor is defined as minimum and maximum collection angles.

The collection angles (θ_{\pm}) can be calculated based on the lens effective aperture a , the object distance d_{obj} and the displacement of the linear sensor from the optical axis x_o .

$$\theta_{\pm} = \tan \left[\frac{a/2 \pm x_o}{d_{obj}} \right] \quad (1)$$

An experiment designed to validate the ray collection condition defined by Eqn. 1 was performed using a series of 25-mm aperture spherical plano-convex (PCX) lenses of varying focal lengths as conveniently characterized test objects. We hypothesized that the resulting LPDI images of the lenses would contain vertical bands of bright regions within the lens apertures corresponding to where the lens surface refracted light into the imaging lens, and that the bandwidth

would increase with lens focal length. Measured results were compared to analytically derived results. This required an expression for γ , the angle of rays emerging from the lens as a function of the angle of the lens exit surface β , see Fig. 9.

$$\gamma = \sin \alpha + \beta (n - 1) \quad (2)$$

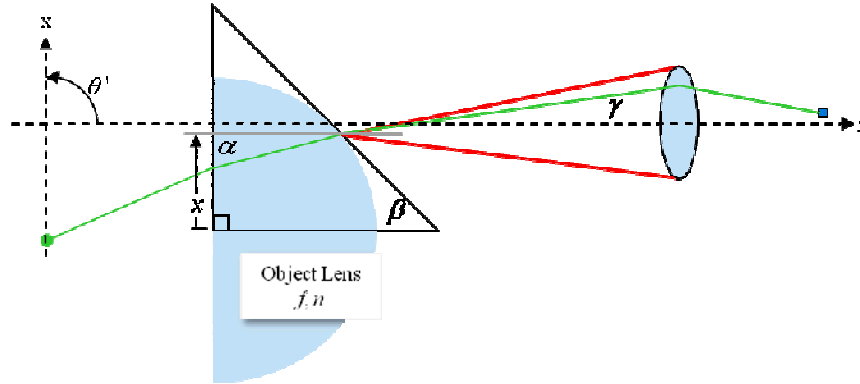


Figure 9: The ray emerging from the object lens forms an angle γ with respect to the optical axis which depends on the test lens surface angle β . Scanning of the object lens in the x -direction defines γ a function of β for a fixed illumination angle of incidence α . The lens angles, β_- and β_+ , are defined as the position of the object lens in the x -axis which causes the emerging ray angle γ to equal the minimum (θ_-) or maximum (θ_+) ray collection angles, see Fig. 8. The distance in x -axis from the lens apex to where the ray emerges from the lens when it is positioned where β_- and β_+ is defined, defines x_- and x_+ , respectively.

For refraction of small angles Eqn. 2 is a suitable approximation that has <1% error for β between ± 130 -mrad. Substitution of γ in Eqn. 2, for θ_{\pm} in Eqn. 1, and solving for β yields β_{\pm} , the angle of lens curvature where light bands should appear (β_-) and disappear (β_+).

$$\beta_{\pm} = \frac{\theta_{\pm} - \sin \alpha_i}{n - 1} \quad (3)$$

Now the equation predicting where in the x -axis bands of light should appear (x_-) and disappear (x_+) within the lens aperture can be solved for as a function of lens focal length f_{obj} using Eqn. 3 and the geometry of the lens based on its radius of curvature R given by the Lensmaker's equation for a PCX lens in air, where $R = f_{obj}(n - 1)$ and n is object lens index.

$$x_{\pm} = \frac{f_{obj}(n - 1)\beta_{\pm}}{\sqrt{1 + \beta_{\pm}^2}} \quad (4)$$

Experimental results for x_- and x_+ , shown in Fig. 10 and 11, agreed with analytical prediction after the parameters a and x_0 were fit to the data.

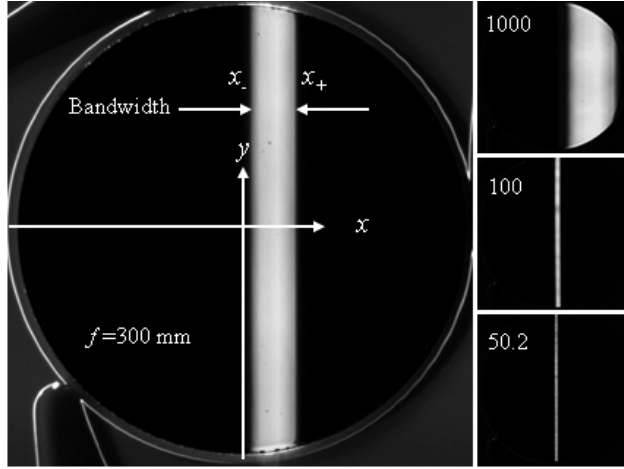


Figure 10: (left) LPDI image of $f=300$ -mm PCX lens. The bands (x_- and x_+) were measured using a 13% signal drop as a consistent edge criteria. Note, the brightness of the band is independent of the y -axis. (right) Focal length lenses measured included: 25.4, 38.1, 50.2 (shown), 62.9, 75, 88.3, 100 (shown), 150, 200, 300 and 1000 mm (shown). Error was significant for lens focal lengths <100 -mm as the bandwidth converged to the pixel size.

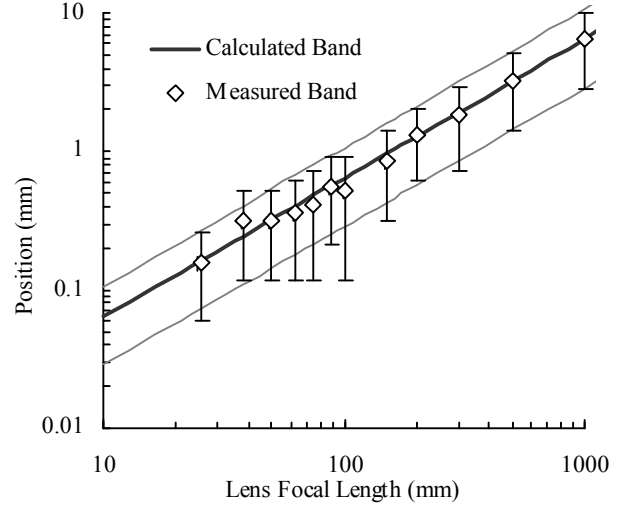


Figure 11: The bold line indicates calculated band center, and lower and upper parallel lighter lines indicate calculated x_- and x_+ respectively. Open diamond points indicate measured band center, y -error indicates measured bandwidth, x_- and x_+ .

5.1 LPDI MODEL

A ray tracing model of LPD applying θ_{\pm} (Eq. 1) and γ (Eq. 2) was developed as a qualitative tool to evaluate FPD detection sensitivity for PSDI measured or artificially defined phase-defect shapes using their effective height profile $h(x,y)$. Recall from Fig. 10 that the PCX lenses showed no measurable signal y -dependence. This indicates that only rays in the xz -plane contribute signal. Accordingly, only the object angle along the x -axis β_x is required for ray computation, which can be extracted from the height function by taking the partial derivative of $h(x,y)$ with respect to x .

$$\beta_x = \tan^{-1} \left(\frac{\partial}{\partial x} h(x,y) \right) \quad (5)$$

This equation implies LPDI is a measurement of the derivative of an objects phase, hence the name, Linescan Phase Differential Imaging.

To validate its relevance as an evaluation tool, modeled results were compared with actual LPDI images. Figure 12 shows the LPDI model results of the FPD from Fig. 1 agreed qualitatively with the measured LPDI image. Both the modeled and measured images show that the sensor detects light imaged from the right side of the defect, corresponding to where the x -derivative of the phase-defect is positive and light is scattered. Conversely, on the left side, where the x -derivative of the phase-defect is negative, light is scattered away from the lens and the region appears dark. This effect has been observed for light source alignments further towards bright-field where the background signal is significant.

The model revealed a limitation of LPDI, that defects with a high degree of symmetry in the x -axis (small x -derivative) produce a low signal. Such defects were discovered to be generated during Magnetorheological finishing (MRF)¹⁰. MRF phase-defects appear as troughs in the surface that are several tens of millimeters in length. When the axis of symmetry of the trough is oriented along the y -axis the defect is easily identified by LPDI, but essentially disappears when rotated parallel to the x -axis, as shown in Figures 13 and 14.

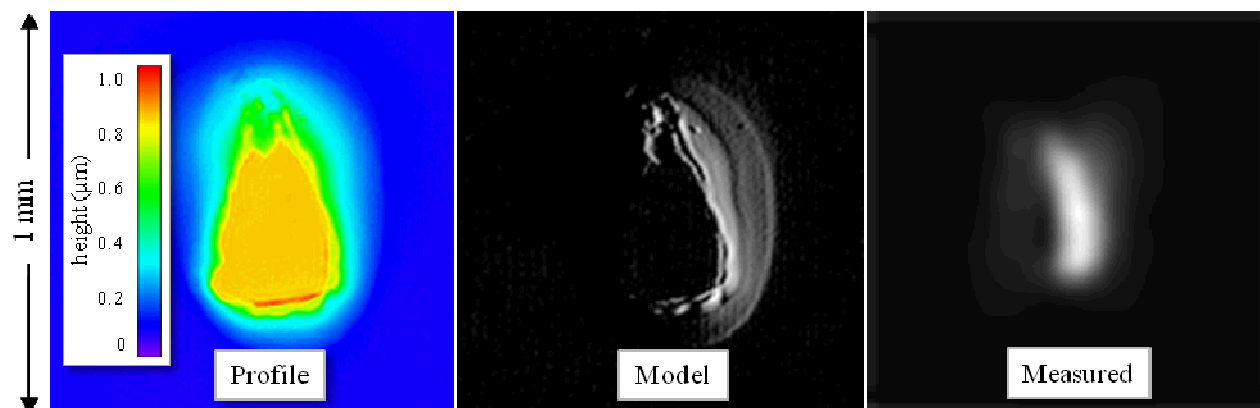


Figure 12: Phase-defect from Fig. 1 is measured by PSDI and modeled to show qualitative agreement with the measured image.

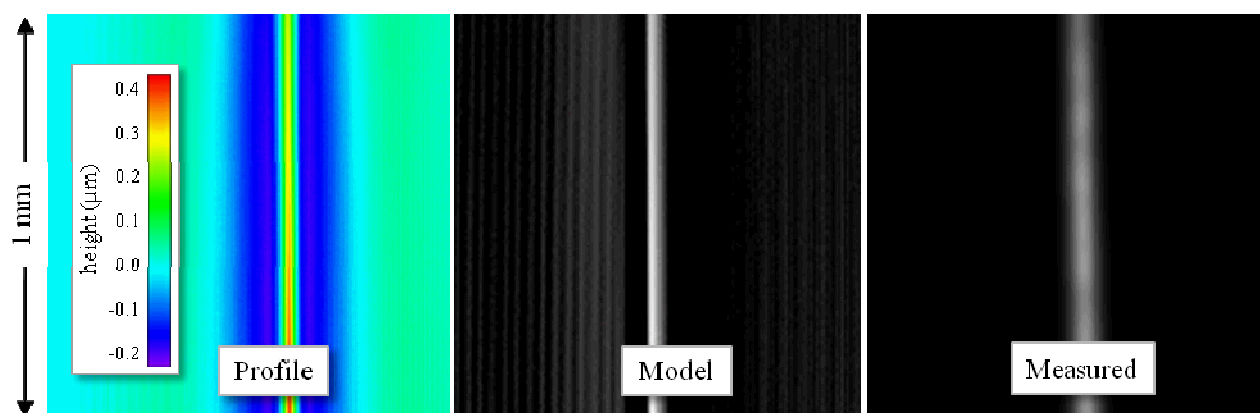


Figure 13: This MRF phase-defect has a strong derivative in the horizontal axis, and as expected produces a strong signal in both the modeled and measured images.

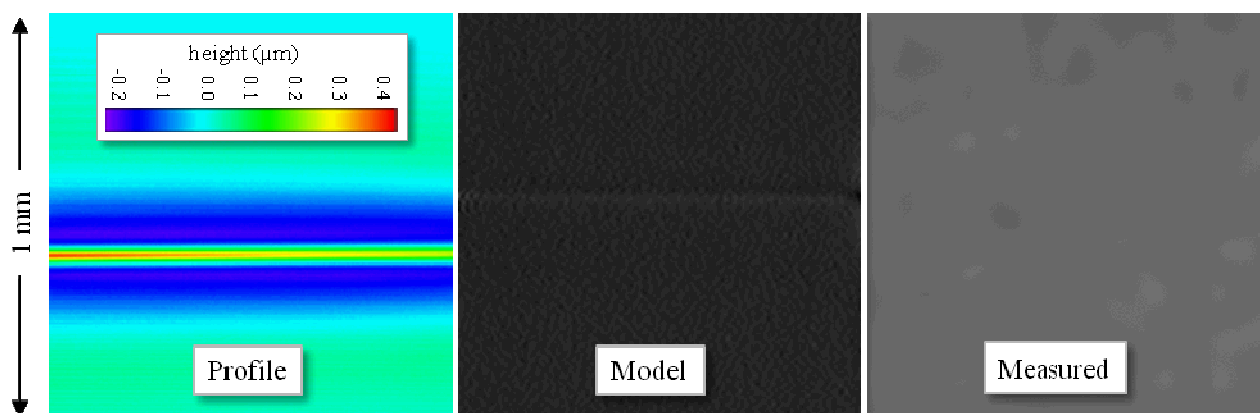


Figure 14: When the MRF defect in Fig. 13 is rotated 90-degrees it disappears in both the LPDI modeled and measured images. Contrast of the modeled and measured images was enhanced to reveal the background signal.

6.0 CONCLUSIONS

LPDI was developed to rapidly identify phase-defect on large-aperture optics used in high-power lasers. Only objects identified by the image analysis software with a P_{max} value that exceeds 2700 are measured with PSDI to assess their fratricidal threat using an empirical laser damage model. The model of LPDI we developed enhanced our understanding of the phase-defect detection mechanism. The LPDI model also revealed that phase-defects with strong symmetry in the light-source axis produce a weak signal due to having a small phase derivative in linescanning direction. Future work could include: extending LPDI capability to lenses, developing an analogy of the LPDI signal to the spatial filtering performed by a frequency domain mask of the phase-defects Fourier transform as a possible way of phase extraction for direct defect assessment. Other applications of LPDI could also be explored.

ACKNOWLEDGEMENTS

The precision opto-mechanical engineering of Robert Bishop and the work in the lab by Larry Platz was vital to the development of LPDI.

REFERENCES

1. C.A. Haynam, P.J. Wegner, J.M. Auerbach, M.W. Bowers, S.N. Dixit, G.V. Erbert, G.M. Heestand, M.A. Henesian, M.R. Hermann, K.S. Jancaitis, K.R. Manes, C.D. Marshall, N.C. Mehta, J. Menapace, E. Moses, J.R. Murray, M.C. Nostrand, C.D. Orth, R. Patterson, R.A. Sacks, M.J. Shaw, M.L. Spaeth, S.B. Sutton, W. H. Williams, C. C. Widmayer, R. K. White, S. T. Yang, and B. M. Van Wonterghem, "National Ignition Facility laser performance status," Proc. Applied Optics Vol. **46** Issue 16 (2007)
2. J.T. Hunt, K.R. Manes, Renard P.A., "Hot Images From Obscurations", Applied Optics **32**, 5973-5982 (1993)
3. M.C. Nostrand, C.J. Cerjan, M.A. Johnson, T. I. Suratwala, T.L. Weiland, W.D. Sell, J.L. Vickers, R.L. Luthi, J.R. Stanley, T.G. Parham, C.B. Thorsness, "Correlation of Laser-induced Damage to Phase Objects in Bulk Fused Silica," Laser-Induced Damage in Optical Materials, G.J. Exarhos, A.H. Guenther, N. Kaiser, K.L. Lewis, M.J. Soileau, C.J. Stolz, Proc. SPIE Vol. **5647** (2005)
4. A.D. Conder, E.T. Alger, S.G. Azevedo, J.J. Chang, S.M. Glenn, L.M. Kegelmeyer, J.A. Liebman, M.L. Spaeth, P.K. Whitman, "Final Optics Damage Inspection (FODI) for the National Ignition Facility", Laser-Induced Damage in Optical Materials, G.J. Exarhos, A.H. Guenther, K.L. Lewis, D. Ristua, M.J. Soileau, C.J. Stolz, Proc. SPIE Vol. **6720** (2008)
5. L.M. Kegelmeyer, P.W. Fonga, S.M. Glenna, J.A. Liebman, "Local Area Signal-to-Noise Ratio (LASNR) algorithm for Image Segmentation," Applications of Digital Image Processing, Andrew G. Tescher, Proc. SPIE Vol. **6696** **66962H** (2007)
6. R. N. Smartt and W. H. Steel, "Theory and application of point-diffraction interferometers", Jpn. J. Appl. Phys. Vol. **14**, 351-356 (1975)
7. R.A. Sacks, M.A. Henesian, S.W. Haney, and J.B. Trenholme, "The PROP92 Fourier beam propagation code," *ICF Annual Report*, UCRL-LR-105821-96, 1996, p. 207
8. C.W. Carr, M.D. Feit, M.C. Nostrand, J.J. Adams, "Technique for qualitative and quantitative measurement of aspects of laser-induced damage import for laser beam propagation", IOP Publishing Vol. **17** 1958-1962 (2006)
9. D. Milam, T.J. Hunt, K.R. Manes and W.H. Williams, "Modeling of filamentation damage induced in silica by 351-nm laser pulse", Laser-Induced Damage in Optical Materials, SPIE Vol. 2966 425-428 (1996)
10. J.A. Menapace, P.J. Davis, W.A. Steele, M.R. Hachkowski, A. Nelson, and K. Xin, "MRF Applications: On the Road to Making Large-Aperture Ultraviolet Laser Resistant Continuous Phase Plates for High-Power Lasers," Laser-Induced Damage in Optical 2006, G. J. Exarhos, A. H. Guenther, K. L. Lewis, D. Ristau, M. J. Soileau, C. J. Stolz, Proc. SPIE Vol. **6403** **64030N** (2007)